E1-2018-18

ACTIVATION MEASUREMENT OF NEUTRON PRODUCTION AND TRANSPORT IN A THICK LEAD TARGET AND A URANIUM BLANKET DURING 4 GeV DEUTERON IRRADIATION

Submitted to "Nuclear Instruments and Methods in Physics Research, Section A"

M. Suchopár [1,2,*], V. Wagner [1,2], O. Svoboda [1], J. Vrzalová [1,2,3], P. Chudoba [1,4], P. Tichý [1,2,3], M. Majerle [1], A. Krása [1,5], A. Kugler [1], J. Adam [1,3], L. Závorka [2,3], A. Baldin [3,6], W. Furman [3], M. Kadykov [3,+], J. Khushvaktov [3], A. Solnyshkin [3], V. Tsoupko-Sitnikov [3], S. Tyutyunnikov [3]

On behalf of the Collaboration
"Energy and Transmutation of Radioactive Waste"

[1] Nuclear Physics Institute of the CAS PRI, Hlavní 130, 250 68 Řež near Prague, Czech Republic
[2] Faculty of Nuclear Sciences and Physical Engineering, Czech Technical University in Prague, Břehová 7, 115 19 Praha 1, Czech Republic
[3] Joint Institute for Nuclear Research, Joliot-Curie 6, 141 980 Dubna, Russian Federation
[4] Faculty of Mathematics and Physics, Charles University, Ke Karlovu 3, 121 16 Praha 2, Czech Republic
[5] Belgian Nuclear Research Centre SCK-CEN, Boeretang 200, 2400 Mol, Belgium
[6] Institute for Advanced Studies "OMEGA", Universitetskaya 19, 141 980 Dubna, Russian Federation
[*] Corresponding author at: Nuclear Physics Institute of the CAS PRI, Hlavní 130, 250 68 Řež near Prague, Czech Republic; tel.: +420 910 256 698;
e-mail address: suchopar@ujf.cas.cz
[+] Deceased.

Сухопар М. и др. (от имени коллаборации "Energy and Transmutation of Radioactive Waste") E1-2018-18

Активационное измерение производства и транспорта нейтронов в массивной свинцовой мишени и урановом бланкете в процессе облучения дейтронами при энергии 4 ГэВ

На нуклотроне ОИЯИ в рамках программы «Энергия плюс трансмутация» проводились эксперименты по облучению массивной свинцовой мишени, окруженной бланкетом из природного урана и полиэтиленовой защитой, пучком дейтронов с энергией 4 ГэВ. Для определения энергетического спектра вторичных нейтронов и его пространственного распределения использовались активационные детекторы. Продукты реакций, образовавшиеся в образцах, идентифицировались с помощью гамма-спектроскопии. Полученные в экспериментах данные сравнивались с расчетами с использованием кода MCNPX.

Работа выполнена в Лаборатории ядерных проблем им. В. П. Джелепова ОИЯИ.

Препринт Объединенного института ядерных исследований. Дубна, 2018

Suchopár M. et al. (on behalf of the Collaboration "Energy and Transmutation of Radioactive Waste") E1-2018-18

Activation Measurement of Neutron Production and Transport in a Thick Lead Target and a Uranium Blanket during 4 GeV Deuteron Irradiation

Several simple accelerator-driven system (ADS) setups were irradiated with relativistic proton and deuteron beams in the last years at the Nuclotron synchrotron site of the Joint Institute for Nuclear Research (JINR) in Dubna, Russia. This paper is dedicated to a 4 GeV deuteron irradiation of a setup called Energy plus Transmutation (E + T), consisting of a lead target, natural uranium blanket, and polyethylene shielding. This paper represents the finalization of data analysis and concludes systematics of the proton and deuteron experiments carried out with the E + T setup. Activation detectors served for monitoring of proton and deuteron beams and for measurements of neutron field distribution in model ADS studies. Products of reactions with thresholds up to 106 MeV as well as non-threshold reactions were observed in the samples. The yields of the produced isotopes were determined using the gamma-ray spectrometry and compared with Monte Carlo simulations performed with the MCNPX transport code.

The investigation has been performed at the Dzhelepov Laboratory of Nuclear Problems, JINR.

Preprint of the Joint Institute for Nuclear Research. Dubna, 2018

1. INTRODUCTION

Spallation reaction as an intensive source of high-energy neutrons has been studied with an increasing interest in the last decades. These studies are motivated by the need of high-energy, intensive neutron fluxes for material research, transmutation of nuclear waste or production of nuclear fuel from non-fissile isotopes [1]. With great progress in accelerator technology, accelerator-driven systems (ADS), due to their inherent safety and other unique properties, seem to be a promising tool for effective nuclear waste incineration [2].

Systematic studies of neutron production, transport, and multiplication in spallation targets irradiated with relativistic proton, deuteron, and light ion beams have been carried out at the JINR Nuclotron accelerator facility. Use of various target and blanket materials, component geometries, and moderator compositions enables one to study their influence on produced neutron field. Moreover, these simple and more complex systems can serve for benchmark studies of Monte Carlo particle transport codes.

The subcritical assembly called Energy plus Transmutation (E + T) is a system of a thick lead target surrounded by a natural uranium blanket and a polyethylene moderator-reflector and wooden biological shielding. First, this experimental setup was irradiated with proton beams in the energy range 0.7–2.0 GeV [3–6, 9, 11, 12]. Next logical step in the systematic studies of spallation reactions were experiments with a deuteron beam. The E + T setup was irradiated with 1.6–4.0 GeV deuterons. The results of the 1.6 and 2.52 GeV irradiations were published separately [10, 12–15]. In this paper, we focus solely on the results of the 4 GeV irradiation carried out in November 2009.

We studied high-energy neutron field created inside the E + T setup during the 4 GeV deuteron beam irradiation by means of the activation method. The obtained data were used for testing predictions of the MCNPX transport code [31], since the E + T setup was acknowledged as an IAEA benchmark target [17]. Experimental results combined with simulations were also utilized for tests of high-energy neutron cross sections of selected threshold reactions calculated by the TALYS code [32].

2. MATERIALS AND METHODS

2.1. The Energy + Transmutation Setup. The E + T setup consists of a cylindrical lead target (diameter of 84 mm and total length of 480 mm) and a

surrounding subcritical uranium blanket (mass of 206.4 kg of natural uranium). The target and blanket are divided into four sections. Between the sections, there are 8 mm gaps for placement of activation samples and other detectors. Each section contains a lead cylinder 114 mm long and 30 identical natural uranium rods, which are encased in a hexagonal steel container with a wall thickness of 4 mm. The front and back ends of each section are covered with hexagonal aluminium plates 6 mm thick. The four target-blanket sections are mounted along the target axis on a wooden plate of 68 mm thickness, which is moreover covered with a 4 mm thick steel sheet. The uranium rods are hermetically encapsulated in a 1 mm thick aluminium cladding. Each rod has an outside diameter of 36 mm, a length of 104 mm, and a weight of 1.72 kg.

The four target-blanket sections mounted on the wooden plate are placed in a wooden container filled with granulated polyethylene. The polyethylene serves for moderation and reflection of neutrons back to the setup. The inner walls of the polyethylene box are coated with a 1 mm thick cadmium layer for absorption of neutrons thermalized in polyethylene. The floor wall of the polyethylene box is covered by a textolite plate with a thickness of 38 mm. The front and back ends of the setup are open without shielding. Schematic drawing of the experimental setup and locations of the activation detectors inside the E + T assembly are depicted in Fig. 1. A detailed analysis of the influence of different construction parts and uncertainties in their geometrical and physical definitions on the neutron flux inside the setup can be found in [7].

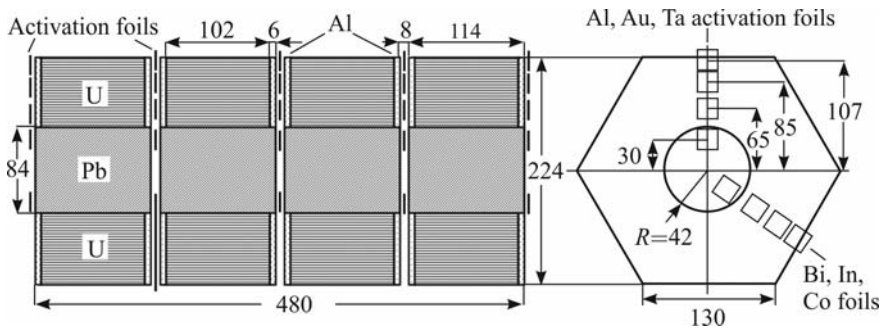

Fig. 1. Side view (left) and front view (right) of the lead target and uranium blanket of the E + T setup. Locations of the activation samples in two radial directions (upward and right-down) are depicted. Dimensions are given in millimeters

2.2. Experimental Method and Data Analysis. Neutron activation method was used to study high-energy neutron production and transport in the system. Activation detectors in the form of thin foils were placed in the gaps between the E + T setup sections to measure the spatial and energy distribution of the inner neutron field, see Fig. 1.

The activation samples were made of aluminium, gold, bismuth, tantalum, indium, and cobalt. These elements were chosen because they are mostly naturally mono-isotopic or one of the isotopes is dominant in natural composition. They also have suitable physical and chemical properties with very few long-lived isotopes produced (in case of bismuth and tantalum) if the foils are intended to be reusable. Further important criteria for selecting these elements were the decay times of the isotopes that were produced in observed (n, xn) threshold reactions. Isotopes with half-lives shorter than roughly an hour or longer than a year were hardly measurable with the available equipment.

The activation samples had a square shape with one side of 20 mm (Al, Au, and Ta samples), 25 mm (Bi samples), and 12.5 mm (In and Co samples). The thickness of the foils varied in the range from 50 μm to 1 mm. Chemical purity of the materials was better than 99.99%. It was tested by the activation method and no significant impurities were found. Average weight of used foils was 0.63 g for Al, 0.36 g for Au, 0.80 g for Ta, 6.54 g for Bi, 0.56 g for In, and 1.36 g for Co foils. Before the irradiation, the foils were wrapped in two layers of thin paper. The outer paper layer minimized contamination of the samples by radioisotopes coming from the setup and it was removed after the irradiation. The inner paper layer prevented the transport of the produced isotopes out of the foil and also between adjoining foils. It was present during every measurement so that possible HPGe detector contamination was excluded.

The activation foils double wrapped in paper were stuck on five plastic plates, mounted on wooden holders and inserted into the slots in the setup. The activation detectors were placed in the setup in two main directions — longitudinal and radial; Al, Au, Ta and Bi, Co, In samples were grouped together. The first group was placed in a row in the upward direction from the target axis (directly on the vertical axis). The second group was placed in the right-down direction in an angle of 30° from the horizontal axis. The plates were put in longitudinal direction at the distances 0, 11.8, 24.0, 36.2, and 48.4 cm from the target beginning, and on each plate the detectors were placed in radial direction at the distances 3.0, 6.0, 8.5, and 10.7 or 11.5 cm from the target axis. List of used samples containing foils placement and dimensions is shown in Table 1.

When the irradiation finished and the period of cooling time (for decrease of the setup radioactivity) was over, the activated detectors were transported in a shielded container to the spectroscopic laboratory in order to measure their γ-activities with HPGe detectors. Almost all the samples were measured at least twice. The first measurement of each sample lasted only a few minutes and all the samples were measured within a few hours. The second measurement was performed up to several days after the irradiation. In this way we detected the maximum of the produced isotopes. Due to about a two-hour span between the end of the irradiation and the start of the measurement, the isotopes with half-lives shorter than approximately one hour could not be observed.

Table 1. Placement of the activation samples in the 4 GeV deuteron experiment at E + T setup

Distance from the target axis, cm	Foil label in the 4 GeV deuteron experiment					
1st plate						
3.0	Al01	Au01	Ta01	Bi1	Co1	In1
6.0	Al02	Au02	Ta02			
8.5	Al03	Au03	Ta03			
10.7	Al04	Au04	Ta04			
2nd plate						
3.0	Al05	Au05	Ta05	Bi2	Co2	In2
6.0	Al06	Au06	Ta06	Bi3	Co3	In3
8.5	Al07	Au07	Ta07	Bi4	Co4	In4
10.7	Al08	Au08	Ta08			
11.5				Bi5	Co5	In5
3rd plate						
3.0	Al09	Au09	Ta09	Bi6	Co6	In6
6.0	Al10	Au10	Ta10			
8.5	Al11	Au11	Ta11			
10.7	Al12	Au12	Ta12			
4th plate						
3.0	Al13	Au13	Ta13	Bi7	Co7	In7
6.0	Al14	Au14	Ta14			
8.5	Al15	Au15	Ta15			
10.7	Al16	Au16	Ta16			
5th plate						
3.0	Al17	Au17	Ta17	Bi8	Co8	In8
6.0	Al18	Au18	Ta18			
8.5	Al19	Au19	Ta19			
10.7	Al20	Au20	Ta20			
Dimensions, mm	20×20	20×20	20×20	25×25	12.5×12.5	12.5×12.5

Complex neutron field was created inside the setup during the irradiation. This field induced various nuclear reactions in the activation samples. Many radioactive nuclei were produced mainly through (n, γ), (n, α), (n, p), and (n, xn) reactions. We measured the yields in each sample from the characteristic γ-ray spectrum emitted during their radioactive decay. The irradiated foils were measured on HPGe detectors of Ortec GMX type (with 28.3 and 32.9% relative efficiencies for the 1332 keV γ-line). The detectors were placed in a lead shielding with the front wall opened for insertion of irradiated samples. This shielding suppressed the natural background substantially. The detector systems

were calibrated before the experiment, and after all measurements the calibration was checked once again to control the calibration stability. The detector systems were calibrated using point-like ^{54}Mn, ^{57}Co, ^{60}Co, ^{88}Y, ^{109}Cd, ^{113}Pb, ^{133}Ba, ^{137}Cs, ^{139}Ce, ^{152}Eu, ^{228}Th, and ^{241}Am standard laboratory sources which have several dozen γ-lines ranging from 80 up to 2700 keV. The accuracy of the peak efficiency determination was $\sim 2\%$ for more distant geometries and $\sim 3\%$ for the nearest geometry.

The acquired γ-ray spectra were analyzed and the net peak areas were determined using the Deimos32 spectroscopy software [16]. All necessary spectroscopic corrections were applied according to Eq. (1) in order to obtain the total number of nuclei of certain isotope. The yield of each isotope was then calculated as a weighted average of multiple γ-lines. The final yield was then normalized to one gram of activation foil material and to one primary beam deuteron using the measured beam intensity so that the results were comparable with previous Energy plus Transmutation experiments. The experimental yields were determined according to the formula

$$N_{\text{yield}}^{\text{exp}} = \frac{S_p \cdot C_{\text{abs}}(E) \cdot B_a}{I_\gamma \cdot \varepsilon_p(E) \cdot \text{COI} \cdot C_g} \frac{t_{\text{real}}}{t_{\text{live}}} \frac{1}{m_{\text{foil}}} \frac{1}{N_d} \frac{e^{(\lambda \cdot t_0)}}{1 - e^{(-\lambda \cdot t_{\text{real}})}} \frac{\lambda \cdot t_{\text{irr}}}{1 - e^{(-\lambda \cdot t_{\text{irr}})}}, \quad (1)$$

where S_p represents peak area, C_{abs}(E) — self-absorption correction, B_a — beam instability correction, I_γ — gamma emission probability, $\varepsilon_p(E)$ — detector peak efficiency, COI — correction for real $\gamma-\gamma$ coincidences, C_g — geometry (non-point like emitter) correction, m_{foil} — mass of foil, N_d — integral deuteron beam flux, t_{real} — real time of measurement, t_{live} — live time of measurement, t_0 — cooling time, t_{irr} — irradiation time, λ — decay constant; $t_{\text{real}}/t_{\text{live}}$ is dead time correction, and the last two fractions represent decay during cooling and measurement and decay during irradiation. Further details concerning the correction factors can be found in [8, 17]. The geometry corrections for every sample size and for each measurement distance from the detector end cap were calculated using MCNPX with models of the used HPGe detectors in the same way as described in [18].

2.3. Beam Parameters Determination. Accurate determination of the beam integral intensity, position and shape is crucial for the experiment evaluation. Firstly, all the experimental isotope yields (Eq. (1)) are normalized to the beam integral. Secondly, the measured beam position and shape are used as input parameters in the MCNPX simulations and impact the calculated isotope yields (Eq. (3)). Significant influence of the beam position on experimental results was observed in previous experiments [17] in the activation detectors placed close to the target axis, where they are influenced by the beam proximity.

The distance from the front of the lead target to the beamline exit window was 690 cm. The beam integral was determined using a square aluminium foil

located at sufficient distance from the setup (nearly 7 m) so that the measurement was not affected by backscattered neutrons from the setup and reaction rates from the activation foils were normalized to this beam monitor. The Al foil was chosen because the cross section of the $^{27}\mathrm{Al}(d,3p2n)^{24}\mathrm{Na}$ reaction is the only one known for deuterons in the region of GeV energies with suitable half-life and energies of γ-lines. Unfortunately, there are only three experimental cross section values for the $^{27}\mathrm{Al}(d,3p2n)^{24}\mathrm{Na}$ reaction in the GeV energy range: (15.25 ± 1.5) mb at 2.33 GeV [19], (14.1 ± 1.3) mb at 6.0 GeV [20] and (14.7 ± 1.2) mb at 7.3 GeV [20]. We made a linear fit on the logarithmic energy scale between these three experimental points and interpolated a cross section value of 14.5 mb for the given energy 4 GeV. The uncertainty of the fit is supposed to be about 10%. The cross section value we used for the beam intensity determination was that from [21], (14.63 ± 1.13) mb at 4 GeV deuteron energy, determined from ratio of proton and deuteron inelastic reaction cross section for production of ^{24}Na on Al. This value is close to that from the linear fit.

After the irradiation, the aluminium foil was folded, wrapped in a paper sheet, and measured on two different HPGe detectors several times in various geometries to suppress the uncertainty coming from detector calibration. We determined the weighted average of the ^{24}Na isotope yield using 1368 and 2754 keV γ-lines. The beam monitoring procedure was similar to that already described more thoroughly in [17, 18]. The same spectroscopic corrections as in Eq. (1) were used in this case. The beam integral N_d was determined according to the following equation:

$$N_d = \frac{N_{\mathrm{yield}} \cdot S \cdot A}{\sigma \cdot N_A}, \tag{2}$$

where N_{yield} — yield of isotope ^{24}Na in the monitor foil, S — area of the foil; A — molar weight; N_A — Avogadro number; σ — $^{27}\mathrm{Al}(d,3p2n)^{24}\mathrm{Na}$ reaction microscopic cross section.

Since the uncertainties caused by the spectroscopic correction factors are relatively small (under 1%), the resulting uncertainties of the yields of all the measured isotopes are dominated by the statistical uncertainties originating from the Gaussian fit of their respective gamma peaks and the systematic uncertainty of the beam integral (Eq. (2)) due to the monitoring reaction cross section known with around 10% accuracy.

The beam intensity was measured independently using concentric Al rings [21] placed on a separate holder close to the square Al foil. In both cases the dimensions of the foils were chosen large enough so that the whole beam profile passed through them.

The irradiation lasted 17.8 h and the beam integral was $(1.99 \pm 0.25) \cdot 10^{13}$ deuterons determined from the square aluminium foil activation [17]. Afterwards, the result was verified by copper activation foils [22], which were initially used for beam position measurement, with our newly obtained relativistic deuteron

cross section data [18]. This analysis confirms results in [17] and refutes the results of the Al concentric rings in [21], which differ by nearly 30% [23, 25]. This way, the originally observed discrepancy between these two independently obtained beam integral values was satisfactorily resolved.

The position and shape of the beam were determined independently by a set of copper activation foils [17] and solid state nuclear track detectors [26, 27] placed on the front side of the setup in the centre of the beam entrance window in the biological shielding. Copper was chosen because in interaction with deuterons a lot of radioactive isotopes are produced, but none of them are produced by neutrons in significant amount (except isotope ^{64}Cu). The copper foil was after the irradiation cut into pieces and every piece was measured separately.

The solid state nuclear track detectors (SSNTD) were used for the beam position and profile determination [28–30]. The SSNTD consisted of two track detectors made of synthetic mica material and a lead foil between them serving as a source of fission fragments which were registered by the track detectors. An elliptical shape and a Gaussian beam profile in X and Y axes were assumed; therefore, two overlapping arrays of SSNTD were attached in front of the target [24]. A fit of the experimental data by Gaussian distribution in horizontal and vertical directions from SSNTD, considered in this case as a more accurate method for the beam profile determination, was afterwards used as input parameters for the particle source in the Monte Carlo simulations. The deuteron beam parameters as measured by different groups are summarized in Table 2.

Table 2. Beam position, shape and integral flux determined during the E + T 4 GeV deuteron irradiation, comparison of data from different groups

Deuteron beam parameters		
	Cu activation foils [17]	SSNTD [26]
X-axis shift, cm	2.4	2.4
Y-axis shift, cm	1.9	1.7
FWHM in X, cm	1.5	2.1
FWHM in Y, cm	1.8	1.8
Deuteron beam fluence, 10^{13}		
Square Al foil [17]	Concentric Al rings [21]	Final (Al + Cu)
1.99 ± 0.25	1.37 ± 0.19	1.99 ± 0.25

3. EXPERIMENTAL RESULTS

3.1. Isotope Yields in Activation Materials. Our profound analysis enabled us to determine the yields of isotopes originating from (n, xn) reactions with higher thresholds unseen in the previous deuteron experiments, partly also due to

higher beam energy and intensity. These results include gold isotopes observed directly and indirectly by means of their decay products — platinum and iridium. In the same way we observed produced isotopes of bismuth directly and indirectly by means of their decay products — lead and thallium. Furthermore, we observed not only cobalt isotopes but also manganese and iron isotopes produced in the cobalt samples.

This enhanced analysis comprises reactions up to $(n, 14n)$ on Au with threshold energies up to 106 MeV: ^{190}Au–^{198}Au were determined directly, ^{191}Au also from ^{191}Pt, ^{189}Au only from ^{189}Pt, ^{188}Au from ^{188}Pt and ^{188}Ir, ^{186}Au from ^{186}Pt and ^{186}Ir, ^{184}Au only from ^{184}Ir. We also observed reactions up to $(n, 12n)$ on Bi with threshold energies up to 88 MeV: ^{201}Bi–^{206}Bi were determined directly, ^{201}Bi also from ^{201}Pb and ^{201}Tl, ^{200}Bi from ^{200}Pb and ^{200}Tl, ^{199}Bi only from ^{199}Tl, ^{198}Bi from ^{198}Pb and ^{198}Tl. As regards the cobalt samples, besides isotopes ^{55}Co–^{60}Co coming from reactions (n, γ) to $(n, 5n)$, we observed additional isotopes ^{52}Mn, ^{54}Mn, and ^{56}Mn produced via $(n, xn + \alpha)$ and $(n, xn + yp)$ reactions, as well as isotopes ^{52}Fe and ^{55}Fe originating from $(n, xn + yp)$ reactions. We thus observed threshold reactions taking place up to threshold energy 62 MeV (corresponding to ^{52}Fe). In tantalum samples we identified reactions up to $(n, 9n)$ with threshold energies up to 61 MeV (^{173}Ta) and in indium samples reactions up to $(n, 7n)$ with reaction thresholds up to 52 MeV (^{109}In).

Some of the reaction products are created by multiple reaction channels with different threshold energies. For instance, the ^{56}Mn is produced in reaction ^{59}Co$(n, \alpha)^{56}$Mn with zero threshold but also in multiple threshold reactions with lower probabilities and various combinations of neutrons, protons, deuterons, tritons or ^{3}He as emitted particles. It should be noted that the mentioned isotopes are produced in $(p, p+xn)$ and $(d, d+xn)$ reactions as well, but the vast majority of their yields originates from (n, xn) reactions. It was proved by the MCNPX simulations.

We focused on determination of the yields of isotopes produced mainly in (n, xn) and (n, γ) reactions. These yields are proportional to the neutron field in the place of the activation foil. Naturally, the higher the yield of a certain (n, xn) reaction is, the more neutrons with the energy higher than the corresponding threshold have to be contained in the spectrum in that particular place. The yields of observed isotopes normalized per gram of the foil mass and per beam deuteron are shown in the semi-logarithmic scale in Figs. 2–6. The error bars in the graphs involve only uncertainties from the Gaussian fit of the peaks in the spectroscopy program Deimos32 and are hardly visible in the semi-logarithmic scale because these are only a few percent. Uncertainty of the beam integral determination is not included because it may change the absolute values but not the shape of the yield spatial distributions. Since the experimental values were measured in discrete spots in the gaps between the setup sections, lines in the graphs connecting experimental points are drawn only for better readability and

have no real physical meaning. Tabulated experimental data for Figs. 2–6 are summarized in Tables 3–7.

Products of the threshold reactions have their measurable maxima near the first gap which is located at 12 cm from the target beginning. This value does not differ significantly for higher beam energies, although the deuteron range in lead obviously rises. The reason for this comes from the probability of the first collision, which takes place for most of the deuterons in the first 20 cm of the

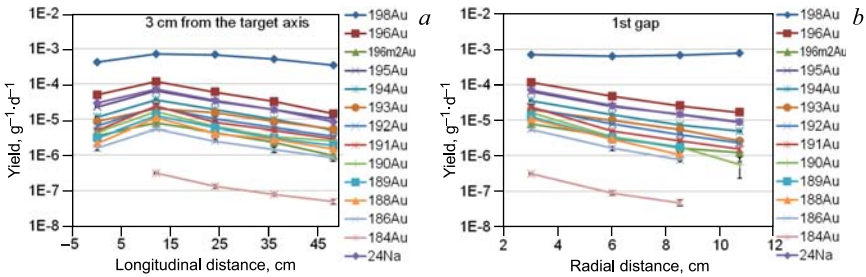

Fig. 2. Experimental yields of observed isotopes in Au and Al foils — (*a*) in longitudinal direction 3 cm over the target axis; (*b*) in radial direction in the first gap of the setup

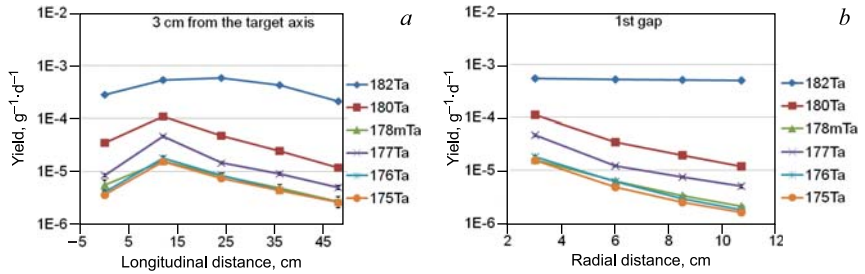

Fig. 3. Experimental yields of observed isotopes in Ta foils — (*a*) in longitudinal direction 3 cm over the target axis; (*b*) in radial direction in the first gap of the setup

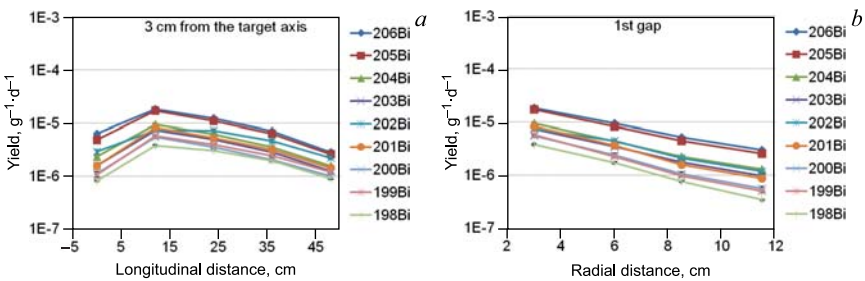

Fig. 4. Experimental yields of observed isotopes in Bi foils — (*a*) in longitudinal direction 3 cm over the target axis; (*b*) in radial direction in the first gap of the setup

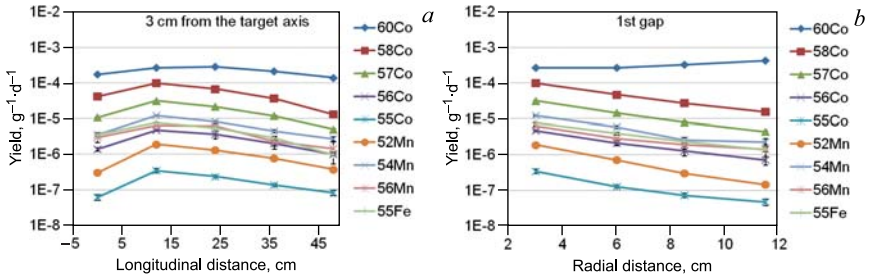

Fig. 5. Experimental yields of observed isotopes in Co foils — (*a*) in longitudinal direction 3 cm over the target axis; (*b*) in radial direction in the first gap of the setup

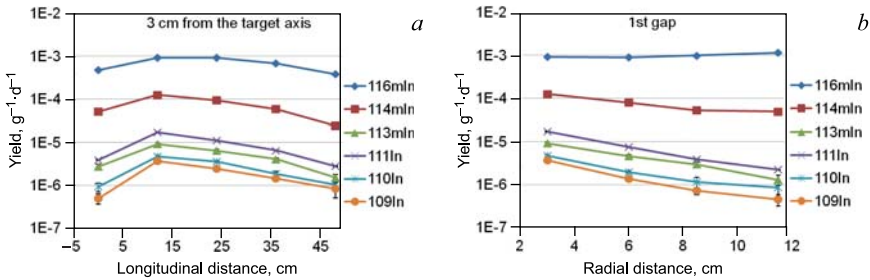

Fig. 6. Experimental yields of observed isotopes in In foils — (*a*) in longitudinal direction 3 cm over the target axis; (*b*) in radial direction in the first gap of the setup

lead target. During the spallation reaction high-energy neutrons are produced in intranuclear cascade mostly to the forward angles, neutrons from high energy fission and evaporation are produced isotropically. These isotropically emitted neutrons cause most of the threshold reactions in the foils placed in front of the lead target.

Non-threshold reactions such as $^{197}\mathrm{Au}(n,\gamma)^{198}\mathrm{Au}$ or $^{181}\mathrm{Ta}(n,\gamma)^{182}\mathrm{Ta}$ are caused by the epithermal and resonance neutrons coming from the biological shielding. High-energy neutrons escaping from the target and blanket are moderated in the polyethylene shielding and some of them are backscattered into the inner volume of the biological shielding. Cadmium layer on the inner walls of the shielding absorbs only neutrons with energies under the cadmium cutoff (~ 0.5 eV). Neutrons with energies higher than this cutoff create inside the biological shielding almost constant field. This field is not as intense as for high-energy neutrons but the yields of, e.g., $^{198}\mathrm{Au}$ or $^{182}\mathrm{Ta}$ are by one to two orders of magnitude higher than the yields of threshold reactions due to the high cross section values of the non-threshold neutron capture reactions.

The field of epithermal and resonance neutrons inside the biological shielding is perturbed only at the beginning and at the end of the setup due to the front

Table 3. Yields of observed isotopes in Au and Al foils, 4 GeV deuteron experiment at E + T setup (part 1)

Foil	^{197}Au						
Reaction	(n,γ)	$(n,2n)$	$(n,2n)$	$(n,3n)$	$(n,4n)$	$(n,5n)$	$(n,6n)$
Product	^{198}Au	^{196}Au	^{196m2}Au	^{195}Au	^{194}Au	^{193}Au	^{192}Au
$E_{\rm thr}$, MeV	0.0	8.1	8.7	14.8	23.3	30.2	38.9
$T_{1/2}$	64.7 h	6.2 d	9.6 h	186.1 d	38 h	17.7 h	4.9 h
R, cm	Isotope yields on plate no. 1 at $L = 0.0$ cm, 10^{-6} g$^{-1}\cdot$ deuteron^{-1}						
3.0	411 ± 4	49.5 ± 1.0	3.64 ± 0.18	22.6 ± 1.2	11.63 ± 0.15	8.8 ± 0.5	6.5 ± 1.1
6.0	410.3 ± 0.5	23.5 ± 0.4	1.54 ± 0.13	12.6 ± 1.2	5.41 ± 0.09	2.2 ± 0.4	2.30 ± 0.17
8.5	458.6 ± 2.4	13.1 ± 0.4	0.92 ± 0.07	7.2 ± 0.8	3.36 ± 0.16	1.31 ± 0.29	1.20 ± 0.06
10.7	513 ± 6	8.44 ± 0.26	0.68 ± 0.08	4.6 ± 0.9	2.18 ± 0.09	0.77 ± 0.26	0.82 ± 0.10
R, cm	Isotope yields on plate no. 2 at $L = 11.8$ cm, 10^{-6} g$^{-1}\cdot$ deuteron^{-1}						
3.0	713 ± 8	118.4 ± 2.8	7.9 ± 0.5	64.1 ± 2.2	36.0 ± 0.5	20.0 ± 0.9	22.5 ± 0.9
6.0	633 ± 6	48.4 ± 0.8	3.42 ± 0.13	24.7 ± 1.5	14.34 ± 0.19	10.2 ± 0.9	8.0 ± 0.5
8.5	682.3 ± 2.1	25.8 ± 0.5	1.70 ± 0.09	14.9 ± 1.3	7.51 ± 0.22	5.6 ± 0.7	4.02 ± 0.22
10.7	779.8 ± 2.2	16.8 ± 0.5	1.23 ± 0.10	9.1 ± 1.3	4.97 ± 0.07	2.7 ± 0.4	2.33 ± 0.16
R, cm	Isotope yields on plate no. 3 at $L = 24.0$ cm, 10^{-6} g$^{-1}\cdot$ deuteron^{-1}						
3.0	672.8 ± 1.3	59.4 ± 2.6	4.38 ± 0.23	32.1 ± 1.3	18.85 ± 0.13	15.3 ± 0.8	10.4 ± 1.3
6.0	627.5 ± 2.1	32.0 ± 0.8	2.26 ± 0.15	16.0 ± 1.2	9.67 ± 0.15	6.6 ± 0.6	5.50 ± 0.23
8.5	665 ± 12	19.5 ± 0.4	1.50 ± 0.14	10.8 ± 1.3	5.90 ± 0.17	4.3 ± 0.5	3.2 ± 0.3
10.7	760 ± 7	13.0 ± 0.4	1.01 ± 0.08	7.5 ± 1.1	4.06 ± 0.13	2.3 ± 0.4	2.25 ± 0.12
R, cm	Isotope yields on plate no. 4 at $L = 36.2$ cm, 10^{-6} g$^{-1}\cdot$ deuteron^{-1}						
3.0	510.0 ± 1.4	32.4 ± 0.7	2.33 ± 0.19	18.8 ± 1.4	9.98 ± 0.19	8.7 ± 0.7	5.97 ± 0.19
6.0	490.8 ± 1.0	18.0 ± 0.4	1.27 ± 0.10	11.7 ± 1.3	5.50 ± 0.11	3.9 ± 0.4	3.34 ± 0.14
8.5	570 ± 4	11.8 ± 0.3	0.88 ± 0.10	7.7 ± 1.0	3.62 ± 0.20	2.3 ± 0.4	2.17 ± 0.10
10.7	663 ± 5	8.25 ± 0.21	0.58 ± 0.15	5.2 ± 1.6	2.59 ± 0.10	2.2 ± 0.5	1.61 ± 0.09
R, cm	Isotope yields on plate no. 5 at $L = 48.4$ cm, 10^{-6} g$^{-1}\cdot$ deuteron^{-1}						
3.0	337.6 ± 1.2	14.41 ± 0.18	0.98 ± 0.09	10.4 ± 1.1	5.02 ± 0.23	5.4 ± 0.4	3.45 ± 0.15
6.0	325.5 ± 1.9	8.21 ± 0.21	0.68 ± 0.09	7.3 ± 1.6	3.13 ± 0.15	2.1 ± 0.4	2.07 ± 0.22
8.5	364.0 ± 1.8	5.16 ± 0.13	0.32 ± 0.05	3.4 ± 1.1	1.82 ± 0.06	1.34 ± 0.27	1.25 ± 0.08
10.7	414.1 ± 2.6	3.68 ± 0.11	0.20 ± 0.05	4.1 ± 1.6	1.36 ± 0.05	1.05 ± 0.30	0.86 ± 0.08

and rear openings in the shielding used for manipulation with the setup parts and for beam entrance window. This is visible in the figures depicting longitudinal distribution of the yields of, e.g., ^{198}Au or ^{182}Ta (see Figs. 2*a* and 3*a*), where the outer points are positioned somewhat lower than the average in between, which is perceptible even on the logarithmic scale.

Table 3. Yields of observed isotopes in Au and Al foils, 4 GeV deuteron experiment at E + T setup (part 2)

Foil	^{197}Au						^{27}Al
Reaction	$(n,7n)$	$(n,8n)$	$(n,9n)$	$(n,10n)$	$(n,12n)$	$(n,14n)$	(n,α)
Product	^{191}Au	^{190}Au	^{189}Au	^{188}Au	^{186}Au	^{184}Au	^{24}Na
$E_{\rm thr}$, MeV	46.0	55.0	62.4	71.9	88.7	106.3	3.2
$T_{1/2}$	3.2 h	42.8 min	28.7 min	8.8 min	10.7 min	53 s	15 h
R, cm	Isotope yields on plate no. 1 at $L = 0.0$ cm, 10^{-6} g$^{-1}\cdot$ deuteron^{-1}						
3.0	4.8 ± 0.3	4.4 ± 2.6	3.1 ± 1.0	2.2 ± 0.5	1.61 ± 0.24	n/a	28.8 ± 0.4
6.0	1.52 ± 0.18	0.5 ± 0.4	n/a	n/a	n/a	n/a	12.50 ± 0.14
8.5	1.11 ± 0.27	0.62 ± 0.22	n/a	n/a	n/a	n/a	7.14 ± 0.12
10.7	1.0 ± 1.0	0.3 ± 0.3	n/a	n/a	n/a	n/a	4.40 ± 0.08
R, cm	Isotope yields on plate no. 2 at $L = 11.8$ cm, 10^{-6} g$^{-1}\cdot$ deuteron^{-1}						
3.0	24 ± 4	16.6 ± 2.2	12.9 ± 1.9	11.2 ± 2.6	5.6 ± 0.5	0.313 ± 0.015	71.2 ± 0.8
6.0	4.97 ± 0.28	3.5 ± 1.2	3.2 ± 0.7	3.0 ± 0.5	1.65 ± 0.21	0.091 ± 0.012	26.5 ± 0.3
8.5	2.71 ± 0.23	1.8 ± 0.5	1.8 ± 0.5	1.1 ± 0.4	0.78 ± 0.08	0.048 ± 0.009	14.64 ± 0.17
10.7	1.6 ± 0.9	0.6 ± 0.3	n/a	n/a	n/a	n/a	8.93 ± 0.12
R, cm	Isotope yields on plate no. 3 at $L = 24.0$ cm, 10^{-6} g$^{-1}\cdot$ deuteron^{-1}						
3.0	8.3 ± 0.3	6.3 ± 1.4	6.0 ± 0.8	4.1 ± 1.3	2.52 ± 0.18	0.132 ± 0.013	34.59 ± 0.22
6.0	3.8 ± 0.3	2.7 ± 0.5	2.4 ± 0.6	2.1 ± 0.6	1.03 ± 0.09	0.054 ± 0.009	18.29 ± 0.21
8.5	2.14 ± 0.29	0.6 ± 0.6	1.44 ± 0.21	n/a	0.66 ± 0.07	n/a	11.03 ± 0.16
10.7	1.39 ± 0.24	0.8 ± 0.4	n/a	n/a	n/a	n/a	7.46 ± 0.09
R, cm	Isotope yields on plate no. 4 at $L = 36.2$ cm, 10^{-6} g$^{-1}\cdot$ deuteron^{-1}						
3.0	5.0 ± 0.4	3.3 ± 0.5	3.0 ± 0.6	2.9 ± 0.7	1.45 ± 0.26	0.079 ± 0.007	18.88 ± 0.25
6.0	2.60 ± 0.22	1.5 ± 0.4	1.8 ± 0.3	n/a	0.72 ± 0.08	0.032 ± 0.008	10.52 ± 0.14
8.5	1.56 ± 0.19	0.8 ± 0.3	0.65 ± 0.20	n/a	0.54 ± 0.08	n/a	8.48 ± 0.12
10.7	1.4 ± 0.6	0.4 ± 0.3	n/a	n/a	n/a	n/a	4.52 ± 0.08
R, cm	Isotope yields on plate no. 5 at $L = 48.4$ cm, 10^{-6} g$^{-1}\cdot$ deuteron^{-1}						
3.0	2.91 ± 0.27	2.6 ± 0.5	1.90 ± 0.21	1.5 ± 0.3	0.85 ± 0.17	0.049 ± 0.007	8.40 ± 0.13
6.0	1.53 ± 0.26	1.4 ± 0.4	n/a	n/a	n/a	n/a	4.75 ± 0.08
8.5	1.09 ± 0.26	0.18 ± 0.26	0.84 ± 0.20	n/a	0.29 ± 0.08	n/a	2.97 ± 0.06
10.7	1.6 ± 0.7	0.59 ± 0.27	n/a	n/a	n/a	n/a	2.11 ± 0.05

In radial direction the yields of threshold reactions are quickly, almost exponentially, decreasing. It is apparent from the products of non-threshold reactions leading to, e.g., ^{198}Au or ^{182}Ta (see Figs. 2*b* and 3*b*) that the epithermal and resonance neutron field is almost homogeneous in radial direction. This homogeneous field can be only slightly perturbed close to the target axis by the difference in

Table 4. Yields of observed isotopes in ^{181}Ta foils, 4 GeV deuteron experiment at E + T setup

Reaction	(n,γ)	$(n,2n)$	$(n,4n)$	$(n,5n)$	$(n,6n)$	$(n,7n)$	$(n,9n)$
Product	^{182}Ta	^{180}Ta	^{178m}Ta	^{177}Ta	^{176}Ta	^{175}Ta	^{173}Ta
$E_{\rm thr}$, MeV	0.0	7.6	22.5	29.2	37.6	44.7	61.0
$T_{1/2}$	114.4 d	8.15 h	2.36 h	56.56 h	8.09 h	10.5 h	3.14 h
R, cm	Isotope yields on plate no. 1 at $L = 0.0$ cm, 10^{-6} g$^{-1}\cdot$ deuteron^{-1}						
3.0	288 ± 10	35.2 ± 2.8	5.6 ± 1.4	8.5 ± 0.5	4.1 ± 0.3	3.63 ± 0.22	1.06 ± 0.27
6.0	258 ± 6	16.3 ± 1.2	2.31 ± 0.10	4.7 ± 0.3	1.69 ± 0.11	1.22 ± 0.11	n/a
8.5	262 ± 5	9.3 ± 0.6	1.33 ± 0.07	3.06 ± 0.25	0.87 ± 0.15	0.68 ± 0.03	n/a
10.7	293.7 ± 1.0	n/a	n/a	n/a	0.26 ± 0.21	n/a	n/a
R, cm	Isotope yields on plate no. 2 at $L = 11.8$ cm, 10^{-6} g$^{-1}\cdot$ deuteron^{-1}						
3.0	550 ± 50	111 ± 5	15.8 ± 0.4	46.4 ± 2.6	18.2 ± 1.4	15.5 ± 0.6	7.8 ± 0.4
6.0	519 ± 10	34.1 ± 2.6	6.2 ± 0.4	12.3 ± 0.6	6.1 ± 0.5	4.82 ± 0.29	1.8 ± 0.3
8.5	514 ± 8	19.3 ± 1.2	3.28 ± 0.14	7.5 ± 0.4	2.91 ± 0.25	2.48 ± 0.15	1.13 ± 0.13
10.7	494 ± 9	11.8 ± 0.5	2.09 ± 0.07	5.0 ± 0.4	1.79 ± 0.21	1.60 ± 0.07	n/a
R, cm	Isotope yields on plate no. 3 at $L = 24.0$ cm, 10^{-6} g$^{-1}\cdot$ deuteron^{-1}						
3.0	595 ± 16	48 ± 6	8.3 ± 1.1	14.6 ± 0.9	8.6 ± 0.7	7.5 ± 0.5	3.27 ± 0.24
6.0	504 ± 8	22.6 ± 2.4	4.4 ± 0.4	7.7 ± 0.5	$4{,}0 \pm 0.3$	3.46 ± 0.20	0.97 ± 0.17
8.5	491 ± 9	14.0 ± 1.6	2.64 ± 0.18	5.7 ± 0.5	2.49 ± 0.20	2.00 ± 0.10	0.62 ± 0.16
10.7	497 ± 9	9.0 ± 0.8	1.68 ± 0.10	5.0 ± 0.5	1.48 ± 0.16	1.39 ± 0.05	n/a
R, cm	Isotope yields on plate no. 4 at $L = 36.2$ cm, 10^{-6} g$^{-1}\cdot$ deuteron^{-1}						
3.0	433 ± 12	24.4 ± 1.9	4.9 ± 0.8	9.1 ± 0.6	4.4 ± 0.4	4.39 ± 0.22	1.89 ± 0.17
6.0	391 ± 8	13.7 ± 1.4	2.8 ± 0.3	5.1 ± 0.5	2.42 ± 0.14	2.26 ± 0.18	n/a
8.5	387 ± 7	8.0 ± 0.7	1.77 ± 0.18	3.8 ± 0.3	1.34 ± 0.16	1.28 ± 0.13	0.51 ± 0.19
10.7	423 ± 8	5.7 ± 0.4	1.35 ± 0.09	4.4 ± 0.3	1.02 ± 0.10	0.98 ± 0.05	n/a
R, cm	Isotope yields on plate no. 5 at $L = 48.4$ cm, 10^{-6} g$^{-1}\cdot$ deuteron^{-1}						
3.0	213 ± 6	11.9 ± 1.1	2.7 ± 0.7	5.0 ± 0.4	2.63 ± 0.22	2.60 ± 0.08	1.00 ± 0.13
6.0	222 ± 5	5.74 ± 0.22	1.45 ± 0.22	2.73 ± 0.20	1.05 ± 0.13	1.04 ± 0.06	n/a
8.5	211 ± 5	3.79 ± 0.22	0.96 ± 0.17	2.10 ± 0.21	0.75 ± 0.11	0.78 ± 0.04	n/a
10.7	246 ± 5	2.4 ± 0.4	0.80 ± 0.15	2.17 ± 0.18	0.59 ± 0.12	0.53 ± 0.05	n/a

neutron absorption in lead and uranium by resonance capture and on the blanket edge by the influence of the moderator-reflector. As regards the threshold reactions, it can be seen that in the radial direction the highest production was always close to the target centre (at $R = 3$ cm from the target axis). In the longitudinal direction the highest fast neutron flux was in the first gap (at $L = 12$ cm from the beginning of the target).

Table 5. Yields of observed isotopes in ^{209}Bi foils, 4 GeV deuteron experiment at E + T setup (part 1)

Reaction	$(n,4n)$	$(n,5n)$	$(n,6n)$	$(n,7n)$	$(n,8n)$
Product	^{206}Bi	^{205}Bi	^{204}Bi	^{203}Bi	^{202}Bi
$E_{\rm thr}$, MeV	22.6	29.6	38.2	45.4	54.3
$T_{1/2}$	6.24 d	15.31 d	11.22 h	11.76 h	1.72 h
L, cm	Longitudinal yields for $R = 3.0$ cm, 10^{-6} g$^{-1}\cdot$ deuteron^{-1}				
0.0	6.35 ± 0.09	4.91 ± 0.16	2.37 ± 0.08	1.59 ± 0.08	2.91 ± 0.24
11.8	18.5 ± 0.4	17.1 ± 0.6	9.5 ± 0.4	7.47 ± 0.14	7.4 ± 0.4
24.0	12.50 ± 0.17	11.1 ± 0.5	6.30 ± 0.25	5.00 ± 0.13	7.2 ± 0.5
36.2	7.13 ± 0.12	6.43 ± 0.27	3.61 ± 0.17	2.90 ± 0.14	4.7 ± 0.3
48.4	2.89 ± 0.04	2.64 ± 0.15	1.57 ± 0.06	1.26 ± 0.06	2.23 ± 0.13
R, cm	Radial yields for $L = 11.8$ cm, 10^{-6} g$^{-1}\cdot$ deuteron^{-1}				
3.0	18.5 ± 0.4	17.1 ± 0.6	9.5 ± 0.4	7.47 ± 0.14	7.4 ± 0.4
6.0	9.49 ± 0.20	8.3 ± 0.5	4.34 ± 0.18	3.50 ± 0.10	4.4 ± 0.3
8.5	5.17 ± 0.07	4.45 ± 0.17	2.23 ± 0.10	1.79 ± 0.06	2.12 ± 0.22
11.5	2.98 ± 0.05	2.55 ± 0.10	1.29 ± 0.05	0.98 ± 0.06	1.19 ± 0.12

Table 5. Yields of observed isotopes in ^{209}Bi foils, 4 GeV deuteron experiment at E + T setup (part 2)

Reaction	$(n,9n)$	$(n,10n)$	$(n,11n)$	$(n,12n)$
Product	^{201}Bi	^{200}Bi	^{199}Bi	^{198}Bi
$E_{\rm thr}$, MeV	61.7	70.9	78.6	88.1
$T_{1/2}$	1.8 h	36.4 min	27 min	10.3 min
L, cm	Longitudinal yields for $R = 3.0$ cm, 10^{-6} g$^{-1}\cdot$ deuteron^{-1}			
0.0	1.59 ± 0.03	1.10 ± 0.14	1.06 ± 0.05	0.82 ± 0.02
11.8	8.27 ± 0.09	5.6 ± 0.4	5.89 ± 0.16	3.86 ± 0.15
24.0	5.38 ± 0.06	3.58 ± 0.25	3.96 ± 0.15	3.07 ± 0.09
36.2	3.18 ± 0.05	2.07 ± 0.16	2.46 ± 0.12	1.97 ± 0.05
48.4	1.44 ± 0.02	1.01 ± 0.08	1.23 ± 0.06	0.91 ± 0.03
R, cm	Radial yields for $L = 11.8$ cm, 10^{-6} g$^{-1}\cdot$ deuteron^{-1}			
3.0	8.27 ± 0.09	5.6 ± 0.4	5.89 ± 0.16	3.86 ± 0.15
6.0	3.63 ± 0.05	2.41 ± 0.25	2.26 ± 0.07	1.72 ± 0.07
8.5	1.59 ± 0.03	1.08 ± 0.10	0.98 ± 0.05	0.77 ± 0.03
11.5	0.87 ± 0.02	0.56 ± 0.06	0.50 ± 0.03	0.34 ± 0.01

Table 6. Yields of observed isotopes in ^{59}Co foils, 4 GeV deuteron experiment at E + T setup (part 1)

Reaction	(n,γ)	$(n,2n)$	$(n,3n)$	$(n,4n)$	$(n,5n)$
Product	^{60}Co	^{58}Co	^{57}Co	^{56}Co	^{55}Co
$E_{\rm thr}$, MeV	0	10.6	19.4	30.9	41.2
$T_{1/2}$	5.27 y	70.86 d	271.8 d	77.27 d	17.53 h
L, cm	Longitudinal yields for $R = 3.0$ cm, 10^{-6} g$^{-1}\cdot$ deuteron^{-1}				
0.0	175 ± 4	41.8 ± 1.0	10.81 ± 0.25	1.38 ± 0.15	0.062 ± 0.012
11.8	269 ± 6	100 ± 7	32.0 ± 0.4	4.73 ± 0.22	0.35 ± 0.04
24.0	286 ± 6	68.5 ± 1.4	21.7 ± 0.4	3.7 ± 1.0	0.236 ± 0.019
36.2	216 ± 5	37.3 ± 0.7	12.10 ± 0.27	2.0 ± 0.3	0.135 ± 0.012
48.4	142 ± 4	13.24 ± 0.26	4.99 ± 0.18	1.02 ± 0.12	0.083 ± 0.015
R, cm	Radial yields for $L = 11.8$ cm, 10^{-6} g$^{-1}\cdot$ deuteron^{-1}				
3.0	269 ± 6	100 ± 7	32.0 ± 0.4	4.73 ± 0.22	0.35 ± 0.04
6.0	273 ± 6	47.6 ± 0.9	14.9 ± 0.3	2.2 ± 0.4	0.128 ± 0.013
8.5	334 ± 7	27.5 ± 0.9	8.1 ± 0.4	1.3 ± 0.4	0.073 ± 0.009
11.5	431 ± 8	15.5 ± 0.3	4.43 ± 0.25	0.72 ± 0.20	0.047 ± 0.010

Table 6. Yields of observed isotopes in ^{59}Co foils, 4 GeV deuteron experiment at E + T setup (part 2)

Reaction	$(n,4n+\alpha)$	$(n,2n+\alpha)$	(n,α)	$(n,2n+t)$	$(n,5n+t)$
Product	^{52}Mn	^{54}Mn	^{56}Mn	^{55}Fe	^{52}Fe
$E_{\rm thr}$, MeV	38.8	17.5	0	28.2	62.2
$T_{1/2}$	5.59 d	312.3 d	2.58 h	2.73 y	8.28 h
L, cm	Longitudinal yields for $R = 3.0$ cm, 10^{-6} g$^{-1}\cdot$ deuteron^{-1}				
0.0	0.300 ± 0.010	3.5 ± 0.5	3.0 ± 0.9	3.56 ± 0.27	0.039 ± 0.023
11.8	1.914 ± 0.029	12.3 ± 0.7	6.34 ± 0.13	7.80 ± 0.19	0.088 ± 0.026
24.0	1.319 ± 0.023	8.4 ± 0.6	6.3 ± 1.1	5.34 ± 0.16	0.05 ± 0.03
36.2	0.765 ± 0.020	4.5 ± 0.5	2.3 ± 0.9	2.84 ± 0.28	n/a
48.4	0.377 ± 0.011	2.7 ± 0.4	1.5 ± 0.9	0.96 ± 0.07	0.06 ± 0.03
R, cm	Radial yields for $L = 11.8$ cm, 10^{-6} g$^{-1}\cdot$ deuteron^{-1}				
3.0	1.914 ± 0.029	12.3 ± 0.7	6.34 ± 0.13	7.80 ± 0.19	0.088 ± 0.026
6.0	0.714 ± 0.026	6.0 ± 0.6	2.9 ± 0.8	4.0 ± 0.3	n/a
8.5	0.305 ± 0.011	2.6 ± 0.5	2.0 ± 0.5	2.36 ± 0.27	n/a
11.5	0.148 ± 0.009	2.3 ± 0.6	1.5 ± 0.6	1.38 ± 0.15	0.039 ± 0.025

3.2. Ratios of Yields for Different Reaction Thresholds. Ratios of the yields of various threshold reactions measured in front of the target (at $L = 0$ cm) and behind the target (at $L = 48$ cm) in radial direction 3 cm over the target axis are plotted as a function of their threshold energy in Fig. 7*a*. We observed a clear

Table 7. Yields of observed isotopes in ^{115}In foils, 4 GeV deuteron experiment at E + T setup

Reaction	(n,γ)	(n,n')	$(n,2n)$	$(n,3n)$	$(n,5n)$	$(n,6n)$	$(n,7n)$
Product	^{116m}In	^{115m}In	^{114m}In	^{113m}In	^{111}In	^{110}In	^{109}In
$E_{\rm thr}$, MeV	0	0.34	9.3	16.9	33.7	43.8	51.9
$T_{1/2}$	54.3 min	4.5 h	49.5 d	1.7 h	2.8 d	4.9 h	4.2 h
L, cm	Longitudinal yields for $R = 3.0$ cm, 10^{-6} g$^{-1}\cdot$ deuteron^{-1}						
0.0	484 ± 8	78 ± 7	51 ± 3	2.8 ± 0.3	3.96 ± 0.07	0.93 ± 0.21	0.49 ± 0.13
11.8	939 ± 13	225 ± 14	126 ± 7	9.4 ± 0.5	17.4 ± 0.4	4.81 ± 0.25	3.71 ± 0.17
24.0	924 ± 19	159 ± 15	95 ± 4	6.5 ± 0.5	11.3 ± 0.3	3.62 ± 0.24	2.48 ± 0.24
36.2	690 ± 12	86 ± 9	59 ± 3	4.1 ± 0.3	6.56 ± 0.07	1.9 ± 0.3	1.47 ± 0.15
48.4	387 ± 6	25.4 ± 1.4	24.3 ± 1.6	1.52 ± 0.29	2.82 ± 0.05	1.03 ± 0.11	0.9 ± 0.3
R, cm	Radial yields for $L = 11.8$ cm, 10^{-6} g$^{-1}\cdot$ deuteron^{-1}						
3.0	939 ± 13	225 ± 14	126 ± 7	9.4 ± 0.5	17.4 ± 0.4	4.81 ± 0.25	3.71 ± 0.17
6.0	912 ± 16	123 ± 9	80 ± 4	4.6 ± 0.4	7.55 ± 0.08	1.99 ± 0.14	1.37 ± 0.14
8.5	1000 ± 14	79 ± 6	53 ± 7	3.0 ± 0.4	3.96 ± 0.11	1.2 ± 0.3	0.72 ± 0.13
11.5	1164 ± 21	44 ± 4	49 ± 6	1.3 ± 0.4	2.24 ± 0.05	0.9 ± 0.3	0.45 ± 0.14

trend showing a decrease of the ratio with rising threshold energy from ≈ 3 at 8–10 MeV down to ≈ 1 above 40 MeV. This means that the difference in neutron flux in front of and behind the target is smaller for neutron energies higher than approximately 40 MeV.

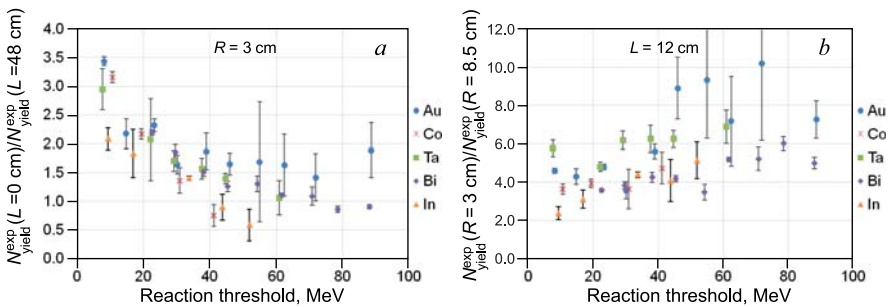

Fig. 7. (*a*) Ratios of experimental yields in front of the target (at $L = 0$ cm) and behind the target (at $L = 48$ cm) 3 cm over the target axis as a function of threshold energy. (*b*) Ratios of experimental yields in the first gap of the setup at $R = 3.0$ cm and at $R = 8.5$ cm as a function of threshold energy

This difference stems from the probability of the first interaction, respectively, spallation reaction. Neutron field inside the setup is a complex mixture of spallation, fission, moderated, and back-scattered neutrons. Fast neutron flux has its measurable maximum at around 12 cm from the target beginning. Neutrons with higher energies come from the intranuclear phase of the spallation reaction and are emitted mainly in forward direction, in contrast to the fast neutrons below 40 MeV, which originate from the evaporation and fission phase of the spallation reaction and are emitted isotropically. Combination of the spallation probability and various sources of neutrons in spallation reaction causes the observed difference in the front to rear yield ratio for the threshold energy below and above approximately 40 MeV.

Ratios in radial direction (at $L = 12$ cm from the target beginning) between the reaction yields in foils at $R = 3$ cm and $R = 8.5$ cm from the target axis in dependence on their threshold energy are shown in Fig. 7*b*. This ratio increases with the rising threshold energy. This means the share of the high-energy neutrons is smaller at further radial distances from the target. This behavior originates from the course of spallation reaction. Neutrons with higher energies are produced mainly in intranuclear cascade and are emitted to forward angles, so they can hardly propagate far from the target in radial direction.

3.3. Spectral Indices. We also compared yields of reactions with different thresholds (^{194}Au/^{196}Au and ^{192}Au/^{196}Au, respectively ^{178m}Ta/^{180}Ta and ^{176}Ta/^{180}Ta) in the same sample. We observed noticeable spectrum hardening towards the end of the target (see Figs. 8–10). The used comparison method is in principle similar to the one presented in the previous paragraph except the fact that this time the yields of different threshold reactions are compared across every sample. The share of neutrons above certain threshold energy is here represented in the ratio of two reactions with different thresholds. The observed spectrum hardening along the target is specific for the course of the spallation reaction where the high-energy neutron production is pronounced into the forward direction.

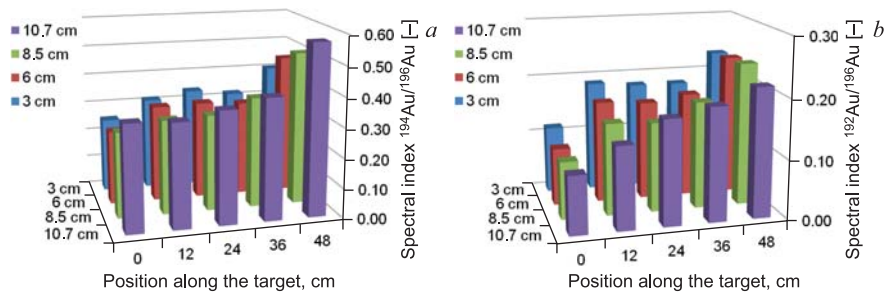

Fig. 8. Experimental spectral indices and demonstration of neutron spectra hardening along the target — (*a*) ratio between ^{194}Au and ^{196}Au; (*b*) ratio between ^{192}Au and ^{196}Au

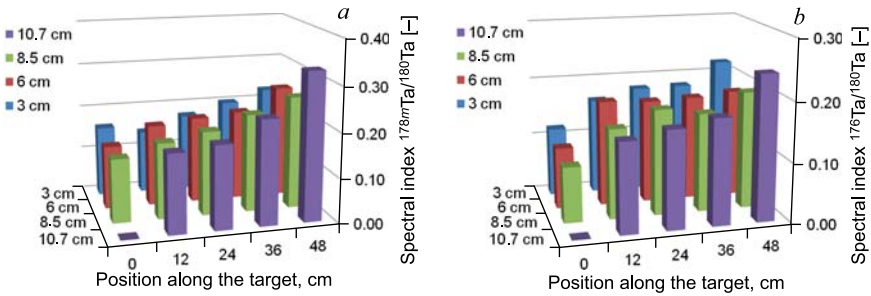

Fig. 9. Experimental spectral indices and demonstration of neutron spectra hardening along the target — (*a*) ratio between ^{178m}Ta and ^{180}Ta; (*b*) ratio between ^{176}Ta and ^{180}Ta

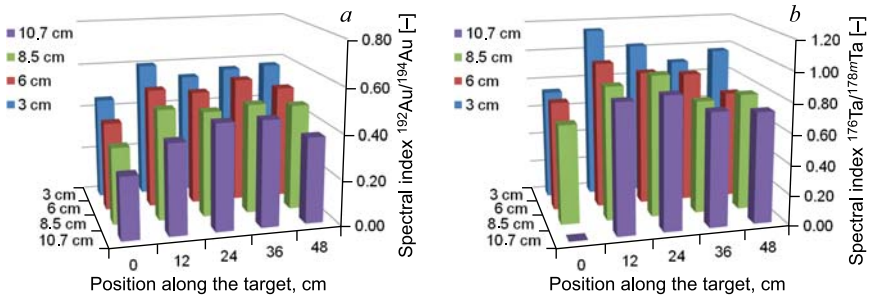

Fig. 10. Experimental spectral indices and demonstration of neutron spectra hardening along the target — (*a*) ratio between ^{192}Au and ^{194}Au; (*b*) ratio between ^{176}Ta and ^{178m}Ta

4. SIMULATION PROCEDURE

We simulated the isotope production in threshold (n, xn) reactions as well as in non-threshold (n, γ) reactions in activation samples to be able to compare them with the experimental results. A detailed description of the complex geometry was created containing the segmented lead target, uranium rod blanket, polyethylene and wooden shielding, all metal frames, shells, and support structures. Description of small volumes representing the activation detectors was added to this geometry model exactly as they were placed in the actual experiment.

The Monte Carlo simulations of the yields of activation reactions in the samples were performed with the MCNPX code version 2.7.0 [31]. Standard cross section library ENDF/B-VII.1 [33] included in the MCNPX code package was used for the simulations coupled with the INCL4.2 intranuclear cascade [34] and ABLAv3 fission-evaporation [35] models for the primary beam interaction and high-energy particle transport. The simulations were also computed using the alternative CEM03.03 [36] and LAQGSM03.03 [36] models (the differences are

discussed in section 5.2). Microscopic cross sections of all considered threshold reactions were calculated using the TALYS code version 1.6 [32] and 1.8 alike with default parameters of the level density models (Constant Temperature Model (CTM) + Fermi Gas Model (FGM)) [32].

The yields of non-threshold reactions were calculated directly by the MCNPX code with data present in the evaluated cross section library ENDF/B-VII.1. For threshold reactions the situation is more complicated because of the missing cross sections for (n, xn) reactions of higher order in the evaluated data libraries. The available data are usually constrained by the $(n, 4n)$ reaction and limited by upper energy of the library because the MCNPX tallies commonly used for direct folding of the spectral fluxes and excitation functions do not score in models physics regime. This issue was solved in the following manner.

The simulated yields were obtained by folding of the reaction cross sections leading to the examined isotopes calculated by TALYS (in 1 MeV energy bins up to 200 MeV) and MCNPX (in 50 MeV energy bins from 200 MeV up to the primary beam energy) with neutron, proton, deuteron, and charged pion spectral fluxes computed by MCNPX in the volumes corresponding to the specific detector positions during the irradiation. The folding of spectral fluxes and threshold reactions cross sections was made according to the following equation:

$$N_{\mathrm{yield}}^{\mathrm{sim}} = \frac{1}{A_r m_u} \sum_{i=n,p,d,\pi} \int_0^{E_{\mathrm{beam}}} \varphi_i(E) \cdot \sigma_i(E)\, dE, \tag{3}$$

where A_r is the specific atomic mass of the element which the foil was made of and m_u is the unified atomic mass unit.

The contribution of various particle types to the total isotope production can vary depending on the sample position in the setup. The contribution to the total reaction yield is produced mainly by neutrons, considerably less by protons, and to a certain extent by deuterons (near the beam axis and close to the target beginning); contribution by charged pions was also considered although negligible; contribution by other particles can be omitted being on the level of the simulation uncertainties.

5. COMPARISON OF EXPERIMENTAL RESULTS WITH SIMULATIONS

5.1. Experiment-to-Simulation Ratios. Experiment-to-simulation ratios of the yields of the observed isotopes are shown in Figs. 11–15. The simulated threshold reaction yields in these charts were obtained by folding the respective excitation functions calculated using TALYS v1.6 with spectral fluxes calculated

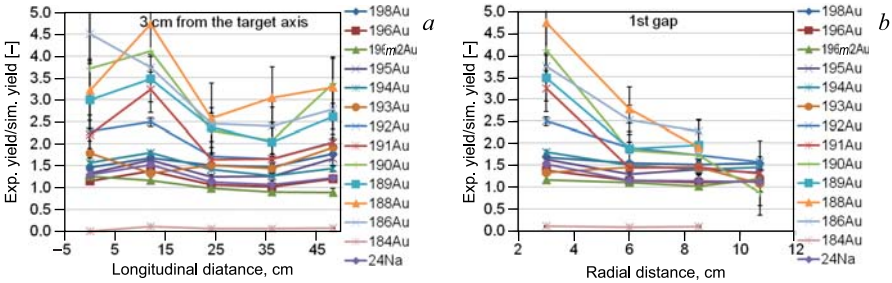

Fig. 11. Ratios of experimental and simulated (MCNPX INCL4 + ABLA) yields in the Au and Al samples — (*a*) in longitudinal direction 3 cm over the target axis; (*b*) in radial direction in the first gap of the setup

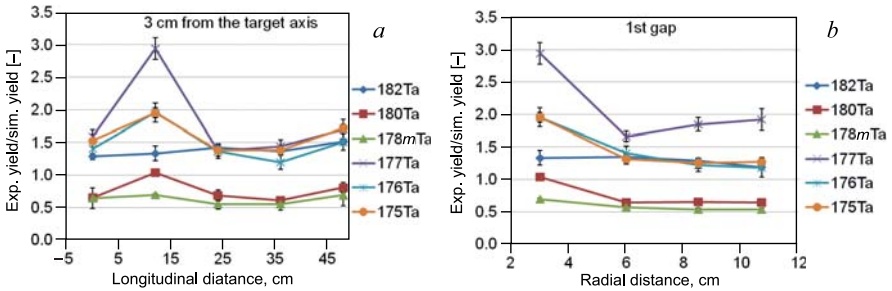

Fig. 12. Ratios of experimental and simulated (MCNPX INCL4 + ABLA) yields in the Ta samples — (*a*) in longitudinal direction 3 cm over the target axis; (*b*) in radial direction in the first gap of the setup

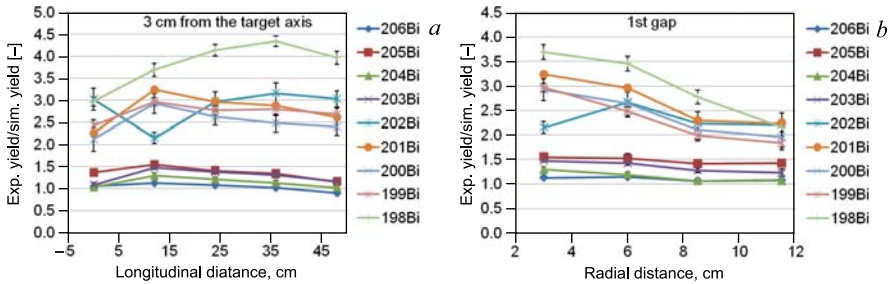

Fig. 13. Ratios of experimental and simulated (MCNPX INCL4 + ABLA) yields in the Bi samples — (*a*) in longitudinal direction 3 cm over the target axis; (*b*) in radial direction in the first gap of the setup

using MCNPX v2.7 with INCL4.2 + ABLAv3 models. The lines in the charts linking the points are present only for better readability. The error bars contain

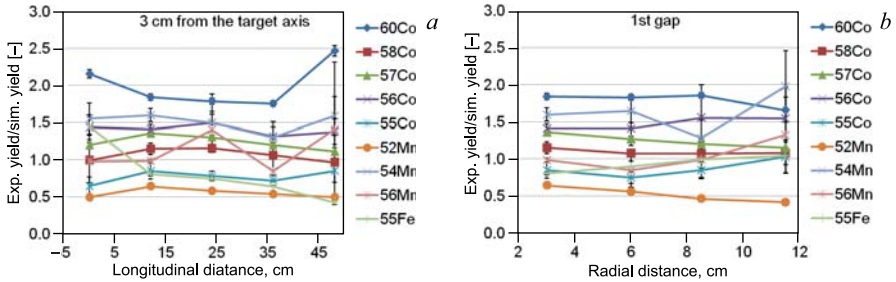

Fig. 14. Ratios of experimental and simulated (MCNPX INCL4 + ABLA) yields in the Co samples — (*a*) in longitudinal direction 3 cm over the target axis; (*b*) in radial direction in the first gap of the setup

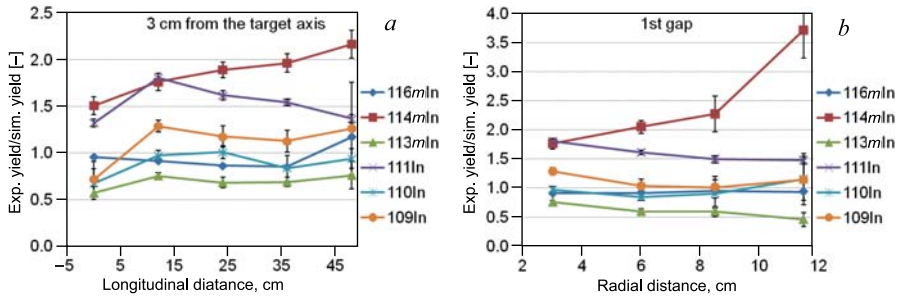

Fig. 15. Ratios of experimental and simulated (MCNPX INCL4 + ABLA) yields in the In samples — (*a*) in longitudinal direction 3 cm over the target axis; (*b*) in radial direction in the first gap of the setup

only uncertainties of the counting statistics of the gamma-ray peaks and statistical uncertainties of the MCNPX simulations, because the main purpose of this comparison is to assess the relative differences between various isotopes and different measurement points. Some uncertainties are the same for all data points, e.g., beam intensity uncertainty, and their involvement would be confusing in this case.

Nevertheless, if absolute values of the experiment-to-simulation ratios are to be compared to one, other uncertainties have to be also involved. Beside the statistical uncertainty from the Deimos32 program, three percent uncertainty from the HPGe detector calibration and spectroscopic corrections has to be included in the experimental yield uncertainty. In the same way, additional uncertainty of at least ten percent from the beam intensity determination needs to be included. These uncertainties are believed to be independent and thus they should be quadratically summed.

The simulated and measured shapes of the longitudinal and radial yields are in good agreement for most of the yields. There are no clear trends that would support the data of an earlier E + T experiment [12] where a steeper simulated decrease of the yields with growing radial distance from the target was observed for beam energies higher than 1.5A GeV.

The absolute values of the experiment-to-simulation ratio depend naturally on the beam intensity determination. The simulations systematically underestimate the experiment as the experiment-to-simulation ratio varies between 1 and 2 in most cases up to a threshold energy of around 60 MeV. This could be caused either by the fact that the absolute values of the maxima in the excitation functions calculated using TALYS are lower than they should be or the spectral flux calculated using MCNPX in place of the foil is underestimated, especially for neutrons with higher energies in comparison to the real neutron flux in the experiment. The foils close to the target axis are also influenced more by the beam if the latter is shifted from the center of the target to its edge.

5.2. Ratios for Different Thresholds. The average experimental-to-simulated yield ratios as a function of reaction threshold energy are plotted in Fig. 16. We can state that the vast majority of the ratios lies between 1 and 2. For the reactions with neutron threshold energies higher than $\sim$55–60 MeV, this ratio starts increasing and reaches values between 2 and 3, which is visible for Au and Bi. This is a sign that either the TALYS code underestimates the absolute values of cross sections for (n, xn) reactions of higher order or the MCPNX code spectra calculation underestimates the number of neutrons with energies above approximately 60 MeV. We have also compared folding of the simulated spectra with reaction cross sections calculated in versions 1.6 and 1.8 of the TALYS code. They give very similar results, which differ only by 1–4%. The ratios calculated with TALYS version 1.6 are generally a little closer to one.

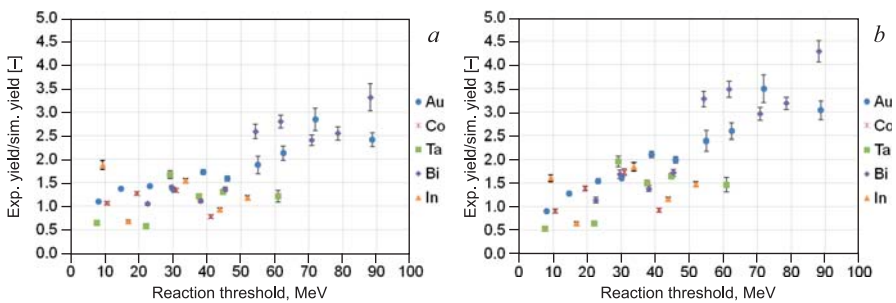

Fig. 16. Average experimental-to-simulated yield ratios as a function of reaction threshold energy folded with TALYS v1.6, calculations performed in MCNPX v2.7 — (*a*) with INCL4.2 + ABLAv3 models; (*b*) with CEM03.03 + LAQSM03.03 models

These experimental yields are compared to the simulations performed with the INCL4.2 + ABLAv3 models (Fig. 16*a*) and the CEM03.03 + LAQGSM03.03 models (Fig. 16*b*). The latter case gives about 10–20% higher values of the experiment-to-simulation ratios than the former, especially for the reactions with a higher threshold.

5.3. Total Neutron Production. The so-called water bath activation foil method [37] is often used for the determination of the integral numbers of neutrons produced in thick targets. The conventional variant of this method uses two basic premises: firstly, neutrons from the source are predominantly contained within the moderator volume; and secondly, it is possible to integrate the measured thermal flux distribution over the water volume with adequate precision. As the latter statement requires the usage of a large-scale grid of activation foils, we have used a new form of this method described in [38], which replaces the flux integration by relating a small-scale set of foil activities to the integral quantity — the integral number of neutrons produced per one beam particle (the so-called neutron multiplicity) n_{sim} obtained by simulation.

Polyethylene in the biological shielding of the E + T setup worked as a water bath — it moderated outgoing neutrons from the blanket. Front and back openings of the biological shielding were not taken into account. We made multiplicity simulations in MCNPX 2.7.0 using all six combinations of the available intranuclear and evaporation models. The simulated multiplicity was calculated as a sum of neutron escape and capture in the setup. In order to calculate the neutron multiplicity, we determined the ratios between experimental and simulated yields of ^{198}Au and ^{182}Ta in gold and tantalum samples, because they were placed close together and have similar cross section for (n,γ) reaction. In addition, we tried to use also cobalt and indium samples for evaluation of (n,γ) reactions leading to ^{60}Co and ^{116m}In. The weighted average over these ratios for each isotope multiplied by the simulated neutron multiplicity gives the experimental neutron multiplicity:

$$n_{\mathrm{total}}^{\mathrm{exp}} = n_{\mathrm{total}}^{\mathrm{sim}} \left\langle \frac{N_{\mathrm{yield}}^{\mathrm{exp}}}{N_{\mathrm{yield}}^{\mathrm{sim}}} \right\rangle . \tag{4}$$

The advantage of this procedure is that $n_{\mathrm{total}}^{\mathrm{exp}}$ is highly insensitive to the simulated value $n_{\mathrm{total}}^{\mathrm{sim}}$ and its uncertainty. Assuming that the MCNPX code describes well the spatial distribution of neutrons as well as the shape of the low-energy part of neutron spectrum and its approximate magnitude, the product of the two terms in Eq. (4) suppresses the dependence on $n_{\mathrm{total}}^{\mathrm{sim}}$ [12, 17].

Results of the neutron multiplicity calculations for the 4 GeV deuteron experiment are summarized in Table 8. The statistical uncertainty of the simulated multiplicities is less than 0.1% for every combination of models and is not stated in the table. On average, the simulated neutron multiplicity of the E + T setup is 108 neutrons per incident 4 GeV deuteron with the difference between mod-

Table 8. Experimental and simulated neutron multiplicities for the 4 GeV E + T experiment

Model	Isotope	$N_{\rm exp}/N_{\rm sim}$	^{198}Au	1.52 ± 0.15	^{182}Ta	1.23 ± 0.12
	$n^{\rm sim}_{\rm total}$	$n_{\rm sim}$/GeV	$n^{\rm exp}_{\rm total}$	$n_{\rm exp}$/GeV	$n^{\rm exp}_{\rm total}$	$n_{\rm exp}$/GeV
Bertini-ABLA	113.4	28.4	172 ± 17	43 ± 4	140 ± 14	35 ± 3
Bertini-Dresner	108.1	27.0	164 ± 16	41 ± 4	133 ± 13	33 ± 3
CEM03	113.0	28.3	171 ± 17	43 ± 4	139 ± 14	35 ± 3
INCL-ABLA	110.8	27.7	168 ± 16	42 ± 4	137 ± 13	34 ± 3
INCL-Dresner	103.9	26.0	158 ± 15	39 ± 4	128 ± 13	32 ± 3
ISABEL-ABLA	107.2	26.8	163 ± 16	41 ± 4	132 ± 13	33 ± 3
ISABEL-Dresner	102.5	25.6	156 ± 15	39 ± 4	126 ± 12	32 ± 3
Average	108.4	27.1	164 ± 16	41 ± 4	134 ± 13	33 ± 3
Model	Isotope	$N_{\rm exp}/N_{\rm sim}$	^{60}Co	1.83 ± 0.19	^{116m}In	1.18 ± 0.12
	$n^{\rm sim}_{\rm total}$	$n_{\rm sim}$/GeV	$n^{\rm exp}_{\rm total}$	$n_{\rm exp}$/GeV	$n^{\rm exp}_{\rm total}$	$n_{\rm exp}$/GeV
Bertini-ABLA	113.4	28.4	207 ± 21	52 ± 5	134 ± 14	34 ± 3
Bertini-Dresner	108.1	27.0	197 ± 20	49 ± 5	128 ± 13	32 ± 3
CEM03	113.0	28.3	207 ± 21	52 ± 5	134 ± 14	34 ± 3
INCL-ABLA	110.8	27.7	202 ± 21	51 ± 5	131 ± 13	33 ± 3
INCL-Dresner	103.9	26.0	190 ± 19	48 ± 5	123 ± 12	31 ± 3
ISABEL-ABLA	107.2	26.8	196 ± 20	49 ± 5	127 ± 13	32 ± 3
ISABEL-Dresner	102.5	25.6	187 ± 19	47 ± 5	121 ± 12	30 ± 3
Average	108.4	27.1	198 ± 20	50 ± 5	128 ± 13	32 ± 3

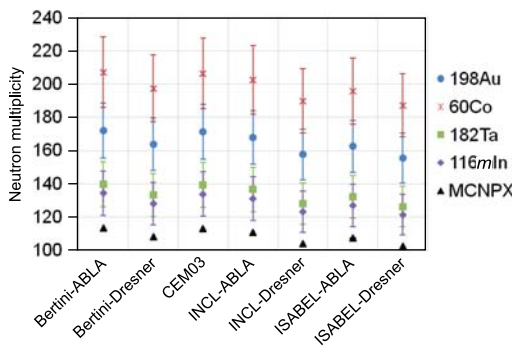

Fig. 17. Experimental and simulated neutron multiplicity for the 4 GeV deuteron E + T experiment. MCNPX calculations were performed with all the available combinations of INC + evaporation models

els giving the lowest and highest simulated multiplicity around 10%. Moreover, we quantified the difference between neutron multiplicity calculated for the centered beam and for the beam with the same FWHM in both directions shifted as in the case of the real experiment. The multiplicity for the shifted beam is by $(3.0 \pm 0.1)\%$ lower than for the centered beam, according to calculation with INCL-ABLA models.

The experimental neutron multiplicity determined with any of the four foil materials gives larger values than the simulations, see Fig. 17. While Ta and In lead to $n^{\mathrm{exp}}_{\mathrm{total}}$ that is about 20% bigger than $n^{\mathrm{sim}}_{\mathrm{total}}$, Co and Au lead to $n^{\mathrm{exp}}_{\mathrm{total}}$ that is 50–80% bigger.

6. CONCLUSIONS

We studied the neutron field produced in the experimental setup called Energy plus Transmutation (E + T) by means of activation detectors made of aluminium, gold, bismuth, tantalum, indium, and cobalt. The E + T setup consisting of a thick lead target, a natural uranium blanket, and a surrounding polyethylene shielding was irradiated with a 4 GeV deuteron beam with an integral flux of $2 \cdot 10^{13}$. The activation foils as well as solid state nuclear track detectors were used for beam monitoring to measure the beam shift, profile, and total fluence. This was the first practical use of new cross sections for relativistic deuteron reactions on copper for determination of deuteron beam integral flux. This paper finished our data analysis and completed the systematics of the proton and deuteron experiments carried out with the E + T setup. We analyzed γ-ray spectra of activated detectors and identified the products of (n, γ), (n, xn), and (n, α) reactions. Thanks to the high energy of the deuteron beam, we observed reactions with extremely high thresholds that have not been observed or used so far in our experiments. It is also a progress from the methodical point of view as the products of reactions with the highest thresholds having too short half-lives were observed indirectly through decays to other nuclides.

We compared the experimental yields of produced nuclides with the results of simulations in the MCNPX and TALYS codes. Relatively good qualitative agreement was found between the experimental and simulated shapes of the yields in both longitudinal and radial directions. However, in absolute terms, the simulations generally underestimate the experimental values. MCNPX describes well the reaction yields for neutrons with lower energies, while for neutrons having higher energies we observed an increase in the difference between experiment and simulation, when their ratio exceeded a factor of two starting from thresholds above 55–60 MeV.

Polyethylene biological shielding in combination with non-threshold reactions enabled us to determine the total number of neutrons produced in the E + T setup per one beam particle. The average simulated neutron multiplicity is between 102 and 113 neutrons per one 4 GeV deuteron, depending on the used combination

of intranuclear and evaporation models. The experimental neutron multiplicity is bigger with a rather large spread of values between 120 and 210 neutrons per one incident deuteron, depending on the foil material used.

Acknowledgements. The authors are grateful to the Veksler and Baldin Laboratory of High Energies and the JINR Nuclotron staff for providing good beam quality and service. We would also like to express our gratitude to the Laboratory of Nuclear Problems staff for providing spectroscopy equipment. This work was financially supported by the Czech Republic JINR grants.

REFERENCES

1. G. Van den Eynde et al. *An updated core design for the multi-purpose irradiation facility MYRRHA*. J. Nucl. Sci. Technol. 52 (2015) 1053–1057. doi:10.1080/00223131.2015.1026860.
2. H. Ait Abderrahim et al. *MYRRHA — A multi-purpose fast spectrum research reactor*. Energy Conversion and Management 63 (2012) 4–10.
3. M. I. Krivopustov et al. *Investigation of neutron spectra and transmutation of ^{129}I,^{237}Np and other nuclides with 1.5 GeV protons from the Dubna nuclotron using the electronuclear installation "Energy plus Transmutation"*. JINR Preprint E1-2004-79 (2004). [http://www1.jinr.ru/Preprints/2004/079(E1-2004-79).pdf]
4. S. R. Hashemi-Nezhad, I. Zhuk, M. Kievets, M. I. Krivopustov, A. N. Sosnin, W. Westmeier, R. Brandt. *Determination of natural uranium fission rate in fast spallation and fission neutron field: An experimental and Monte Carlo study*. Nuclear Instruments and Methods in Physics Research A 591 (2008) 517–529. doi:10.1016/j.nima.2008.02.101.
5. A. Krása et al. *Neutron emission in the spallation reactions of 1 GeV protons on a thick lead target surrounded by uranium blanket*. JINR Preprint E15-2007-81 (2007). [http://www1.jinr.ru/Preprints/2007/081(E15-2007-081).pdf]
6. A. Krása et al. *Neutron production in p +Pb/U at 2 GeV*. JINR Preprint E1-2009-195 (2009). [http://www1.jinr.ru/Preprints/2009/195(E1-2009-195).pdf]
7. M. Majerle et al. *Monte Carlo studies of the "Energy plus Transmutation" system*. JINR Preprint E15-2007-82 (2007). [http://www1.jinr.ru/Preprints/2007/082(E15-2007-82).pdf]
8. M. Majerle et al. *Monte Carlo method in neutron activation analysis*. JINR Preprint E11-2009-178 (2009). [http://www1.jinr.ru/Preprints/2009/178(E11-2009-178).pdf]
9. O. Svoboda et al. *Study of spallation reactions, neutron production and transport in thick lead target and uranium blanket irradiated with 0.7 GeV protons*. JINR Preprint E15-2009-177 (2009). [http://www1.jinr.ru/Preprints/2009/177(E15-2009-177).pdf]
10. O. Svoboda et al. *The study of spallation reactions, neutron production and transport in a thick lead target and uranium blanket during 1.6 and 2.52 GeV deuteron irradiation*. JINR Preprint E15-2011-39 (2011). [http://www1.jinr.ru/Preprints/ 2011/039(E15-2011-39).pdf]
11. F. Křížek, V. Wagner, J. Adam et al. *The study of spallation reactions, neutron production, and transport in a thick lead target and a uranium blanket during 1.5 GeV proton irradiation*. Czech Journal of Physics 56 (3) (2006) 243–252. doi:10.1007/s10582-006-0085-7.

12. A. Krása et al. *Neutron production in a Pb/U-setup irradiated with 0.7–2.5 GeV protons and deuterons*. Nuclear Instruments and Methods in Physics Research A 615 (2010) 70–77. doi:10.1016/j.nima.2010.01.029.

13. M. I. Krivopustov et al. *First results studying the transmutation of ^{129}I,^{237}Np, ^{238}Pu, and ^{239}Pu in the irradiation of an extended ^{nat}U/Pb-assembly with 2.52 GeV deuterons*. Journal of Radioanalytical and Nuclear Chemistry 279 (2009) 567–584. doi:10.1007/s10967-007-7265-1.

14. M. Zamani-Valasiadou et al. *Performance of a Pb-spallation target surrounded by a U-blanket during irradiations with 1.6 and 2.5 GeV deuteron beams: Comparison with relativistic proton beams*. Annals of Nuclear Energy 37 (2010) 241–247. doi:10.1016/j.anucene.2009.10.017.

15. J. Adam, K. Katovský, M. Majerle et al. *A study of nuclear transmutation of Th and $^{\mathrm{nat}}U$ with neutrons produced in a Pb target and U blanket irradiated by 1.6 GeV deuterons*. The European Physical Journal A 43 (2010) 159–173. doi:10.1140/epja/i2010-10909-y.

16. J. Frána. *Program DEIMOS32 for gamma-ray spectra evaluation*. Journal of Radioanalytical and Nuclear Chemistry 257 (2003) 583–587. doi:10.1023/ A:1025448800782.

17. O. Svoboda. *Experimental study of neutron production and transport for ADTT*. Dissertation Thesis. Czech Technical University, Faculty of Nuclear Sciences and Physical Engineering, Prague (2011). [http://ojs.ujf.cas.cz/˜wagner/transmutace/diplomky/PHD_Svoboda.pdf]

18. M. Suchopár et al. *Cross section studies of relativistic deuteron reactions on copper by activation method*. Nuclear Instruments and Methods in Physics Research B 344 (2015) 63–69. doi:10.1016/j.nimb.2014.12.006.

19. J. Banaigs et al. *Détermination de l'intensité d'un faisceau de deutons extrait d'un synchrotron et mesure des sections efficaces des réactions $^{12}C(d,p2n)^{11}C$ et $^{27}Al(d,3p2n)^{24}Na$ á 2,33 GeV*. Nuclear Instruments and Methods in Physics Research 95 (2) (1971) 307–311. doi:10.1016/0029-554X(71)90382-X.

20. P. Kozma and V. V. Yanovski. *Application of BaF_2 scintillator to off-line gamma ray spectroscopy*. Czech Journal of Physics 40 (4) (1990) 393–397. doi:10.1007/BF01597913.

21. W. Westmeier et al. *Experiment S: 4.00 GeV deuterons on E + T*. Technical Report. Internal publication for E + T collaboration (2011).

22. V. Wagner et al. *Nuclear data for advanced nuclear systems*. In Proceedings of Science Baldin ISHEPP XXII (2014) 057. [http://pos.sissa.it/archive/conferences/225/057/Baldin%20ISHEPP%20XXII_057.pdf]

23. J. J. Borger, S. R. Hashemi-Nezhad, D. Alexiev, R. Brandt, W. Westmeier, B. Thomauske, J. Adam, M. Kadykov, S. Tiutiunnikov. *Spatial distribution of thorium fission rate in a fast spallation and fission neutron field: An experimental and Monte Carlo study*. Nuclear Instruments and Methods in Physics Research A 664 (2012) 103–110. doi:10.1016/ j.nima.2011.10.027.

24. J. J. Borger, S. R. Hashemi-Nezhad, D. Alexiev, R. Brandt, W. Westmeier, B. Thomauske, S. Tiutiunikov, M. Kadykov, V. S. Pronskikh, J. Adam. *Studies of the neutron field of the Energy plus Transmutation set-up under 4 GeV deuteron irradiation*. Radiation Measurements 46 (2011) 1765–1769. doi:10.1016/j.radmeas.2011.04.037.

25. J. J. Borger, S. R. Hashemi-Nezhad, D. Alexiev, R. Brandt, W. Westmeier, B. Thomauske, M. Kadykov, S. Tiutiunnikov. *Fission of ^{209}Bi, ^{nat}Pb and ^{197}Au in the particle field of a fast accelerator-driven system*. Annals of Nuclear Energy 53 (2013) 50–58. doi:10.1016/j.anucene.2012.07.029.
26. A. S. Potapenko et al. *Methods and results of the $^{nat}Pb(d, f)$, $^{209}Bi(d, f)$ and $^{209}Bi(d, xnyp)$ reactions cross sections measurements at 1.6 and 4 GeV deuteron beams*. In: ISHEPP XX International Baldin Seminar on High Energy Physics Problems: Relativistic Nuclear Physics and Quantum Chromodynamics. JINR, Dubna, Russia (2010) pp. 282–290.
27. V. V. Sotnikov et al. *Experimental determination of the $^{nat}Pb(d, f)$, $^{209}Bi(d, f)$, $^{209}Bi(d, xnyp)$ nuclear reaction cross sections at 1.6 GeV and 4 GeV deuteron beams*. In: The Third International Conference on Current Problems in Nuclear Physics and Atomic Energy. Institute for Nuclear Research, Kiev, Ukraine (2010) pp. 250–253.
28. S. R. Hashemi-Nezhad, I. V. Zhuk, A. S. Potapenko, M. Kievets, M. I. Krivopustov. *Calibration factors for determination of relativistic particle induced fission rates in ^{nat}U,^{235}U,^{232}Th, ^{nat}Pb and ^{197}Au foils*. Nuclear Instruments and Methods in Physics Research A 664 (2012) 154–160. doi:10.1016/j.nima.2011.10.029.
29. S. R. Hashemi-Nezhad, I. V. Zhuk, A. S. Potapenko, M. I. Krivopustov. *Determination of high-energy proton beam profile using track detectors*. Radiation Measurements 43 (2008) S210–S214. doi:10.1016/j.radmeas.2008.03.074.
30. I. Zhuk, A. Potapenko, S. R. Hashemi-Nezhad, M. I. Krivopustov. *Determination of high-energy deuteron beam profile and spatial distribution of high-energy neutrons in a U/Pb assembly under 1.26 GeV/nucleon deuteron irradiation*. Radiation Measurements 43 (2008) S199–S203. doi:10.1016/j.radmeas.2008.03.057.
31. D. B. Pelowitz, editor. MCNPX User's Manual, Version 2.7.0. LANL report LA-CP-11-00438 (2011).
32. A. J. Koning and D. Rochman. *Modern nuclear data evaluation with the TALYS Code System*. Nuclear Data Sheets 113 (2012) 2841–2934. doi:10.1016/j.nds.2012.11.002.
33. M. B. Chadwick et al. *ENDF/B-VII.1 nuclear data for science and technology: Cross sections, covariances, fission product yields and decay data*. Nuclear Data Sheets 112 (12) (2011) 2887–2996. doi:10.1016/j.nds.2011.11.002.
34. A. Boudard et al. *Intranuclear cascade model for a comprehensive description of spallation reaction data*. Phys. Rev. C 66 (2002) 044615. doi:10.1103/ PhysRevC.66.044615.
35. A. R. Junghans et al. *Projectile-fragment yields as a probe for the collective enhancement in the nuclear level density*. Nuclear Physics A 629 (1998) 635–655. doi:10.1016/S0375-9474(98)00658-7.
36. S. G. Mashnik et al. *CEM03.03 and LAQGSM03.03 event generators for the MCNP6, MCNPX, and MARS15 transport codes*. LANL report LA-UR-08-2931 (2008).
37. K. H. Beckurts, K. Wirtz. Neutron Physics. Springer-Verlag, New York (1964).
38. K. van der Meer et al. *Spallation yields of neutrons produced in thick lead/bismuth targets by protons at incident energies of 420 and 590 MeV*. Nuclear Instruments and Methods in Physics Research B 217 (2004) 202–220. doi:10.1016/j.nimb.2003.10.009.

Received on April 3, 2018.

Редактор *Е. И. Кравченко*

Подписано в печать 14.06.2018.
Формат 60 × 90/16. Бумага офсетная. Печать офсетная.
Усл. печ. л. 2,25. Уч.-изд. л. 2,59. Тираж 275 экз. Заказ № 59418.

Издательский отдел Объединенного института ядерных исследований
141980, г. Дубна, Московская обл., ул. Жолио-Кюри, 6.
E-mail: publish@jinr.ru
www.jinr.ru/publish/